


# FILTRATION EFFICIENCY IN THE RECYCLING PROCESS OF PARTICLE-REINFORCED ALUMINUM ALLOYS USING DIFFERENT FILTER MATERIALS

Johannes Paul Schoß , Benedict Baumann, Andreas Keßler, Michal Szucki and Gotthard Wolf  
 Foundry Institute, TU Bergakademie Freiberg, 09599 Freiberg, Germany

Copyright © 2022 The Author(s)  
<https://doi.org/10.1007/s40962-022-00880-z>

## Abstract

*In this study, filtration of aluminum alloy (Al) with different weight fractions of SiC particles (SiCp) was investigated. Therefore, three different filter materials of 20 pores per inch (ppi) ceramic foam filters (CFF) were tested. A special three-chamber furan mold was used for the casting trials to provide uniform filling and flow conditions for the filtration process. Samples from sections of the gating system, as well as from the filter, were analyzed by optical light microscopy to determine the amount, size, and distribution of SiCp. A scanning electron microscope (SEM) with energy-dispersive X-ray spectroscopy (EDS) was used for obtaining the element distribution in the composite. The filtration efficiency increased by decreasing the weight*

*fraction from 20 to 5% of SiCp and reached a significant particle reduction of over 90%. Investigations of CFFs with a weight fraction of 10% have shown a clogging effect and metal flow interruption through the 20 ppi filter. An oxide layer was detected around the respective SiCp in the EDS. Moreover, a strong accumulation effect was observed, indicated by a steadily flattening curve of the density functions after each additional remelting cycle of the same composite material.*

**Keywords:** metal matrix composites, SiC particles, filtration efficiency, metal melt filtration, recycling

## Introduction

Metal matrix composites (MMCs) are materials consisting of a metal matrix with a reinforcement phase of ceramic particles (SiC, Al<sub>2</sub>O<sub>3</sub>, etc.) or short carbon or ceramic fibers.<sup>1–7</sup> An interesting example of MMCs is Duralcan™. This is an aluminum matrix composite (AMC), which contains particles of aluminum oxide (Al<sub>2</sub>O<sub>3</sub>) or silicon carbide (SiC) in an AlSi9Mg matrix (corresponding to an EN AB-43300 or AA359).<sup>5,6,8,9</sup> The primary production of AMCs can be divided into three industrial-scale processes. The first is stirring or mixing of ceramic particles into molten aluminum (Al) by a patented technology, the second is the melt penetration into a prefabricated foam structure, and the powder metallurgy constitutes the third.<sup>1,5,7,9,10</sup> However, during the manufacturing process, the low wettability between the melt and the ceramic particles must be compensated imperatively in order to generate the proper microstructure of the composite. Therefore, stirring is the most commonly used technique

for AMCs.<sup>1,7,8,10</sup> The composite products are available as casting ingots, extrusion billets, rolling blooms, rolling ingots and can be further processed by casting or forming in press/rolling mills.<sup>1,2,8,9</sup>

Because of the viscosity of the liquid MMC during particle addition, the weight fraction is limited to 30%.<sup>1</sup> The distribution and shape of SiC particles (SiCp) can be adjusted throughout a special centrifugal casting process.<sup>11</sup> An AMC with an initial weight fraction of 10% SiCp can be formed with a contained outer layer of 30% by predefined rotational speeds.<sup>2</sup> However, to obtain the beneficial properties of AMCs, the reinforced particles should be fine and well-distributed.<sup>9</sup> Depending on the type of reinforcement phase, its weight fraction, shape, and distribution, AMCs can combine good tribological properties with high strength and Young's modulus, high wear resistance, high thermal conductivity with low thermal expansion coefficient, and low density (2.8–3.4 g/cm<sup>3</sup>).<sup>1,5,6,9,10,12–16</sup> Lohmüller et al.<sup>12</sup> studied different reinforcement particles on Al and Mg alloys to generate MMCs with a density lower than 2.5 g/cm<sup>3</sup>, and a minimum Young's modulus of 400 GPa. They found that with increasing the weight

fraction of reinforced particles, the specific stiffness ( $E/\rho$ ), and Young's modulus also increased, implying that the particle density influences the stiffness significantly.<sup>12</sup> Due to an exceptional ratio of Young's modulus to density, parts made of AMC exhibit a very high modulus of rigidity and stiffness.<sup>6</sup> Especially in mechanical engineering, those properties are important for the production of components with the highest dimensional accuracy and stability, such as drive spindles, engine cylinders, pistons, cardan shafts, disc and drum brakes, and other elements of the automotive and aerospace industries.<sup>1,6,13,17</sup> For example, AMCs are used for brake systems made of Al2124/SiC/25p in race cars such as Porsche 911.<sup>13</sup> Another application for utilization of AMCs are cardan shafts for the Chevrolet Corvette and Ford Crown Victoria, which are produced by stir casting using an Al alloy with ceramic reinforced  $Al_2O_3$  particles.<sup>13</sup>

The wide range of AMC applications leads to the necessity to provide recyclability of these components after environmental damage or reclamation within the manufacturing process.<sup>8,17</sup> The high amount of scrap must be considered in the global recycling material stream. There is few information available on the recyclability of particle-reinforced AMCs.<sup>17</sup> The global market demand analyses in terms of MMC production volumes and profits showed a steady increase from 5000 to 8000 tons, for the period from 2012 (\$228.7 million) to 2019 (\$357.3 million).<sup>13,18</sup> The compound annual growth rate (CAGR) during this period was around 6.6%,<sup>18</sup> and will remain in the range of 6.4% and 7.0% over the next five years, depending on future forecasts.<sup>19,20</sup> AMCs hold the largest proportion of this market, with 40%.<sup>21</sup> Thereby, SiC is the most prevalent reinforcement material in the global MMC market due to the high demand from the electrical, automotive, transportation, and aerospace industries.<sup>18-21</sup> With further CAGR, the amount of AMC scrap will also increase in the future, which implies that recycling of these materials will become inevitable for saving energy and  $CO_2$  emissions, and using recyclable secondary materials will become more important as well.

If the high amount of scrap can be recycled, the aluminum composite material could have the same properties as the original AMC.<sup>8</sup> Eliasson & Sandström<sup>6</sup> found two options for recycling particle-reinforced composites: remelting the material or reclamation, which means that the particles are separated from the matrix or subsequently reused. Sharma et al.<sup>17</sup> observed that the SiC particles can be recycled by remelting of casting composite scrap using settling trials. They found that the SiC particles settled down immediately at very high rates within the first minutes after remelting them, providing that the settling rate depends on the particle size and weight fraction.<sup>17</sup> In contrast, the simple recycling of scrap or recycled material (such as risers, gating systems, etc.) for the production of particle-reinforced aluminum alloys is rebutted, according to Schuster

et al.<sup>8</sup> Conventional salt and gaseous fluxes cannot be used to clean the molten scrap because they would dewet the SiC particles from the residual melt. Once the SiCp are dewetted, they cannot be readily stirred back into the liquid. Regarding the guidelines: "Duralcan Composite Casting",<sup>22</sup> the scrap and recycled material can be reused in an eleven-step melt bath treatment with an excessive amount of original alloy according to the principle of infinite dilution. Alternatively, the SiC particles can be completely separated and removed by adding fluxes and bath agitation (flushing gas and rotation) using a rotary salt furnace. The dewetted SiC particles float in the molten aluminum with the aid of fluxes and injected argon gas and are potentially available again for the expensive primary production.<sup>8</sup>

In addition, the production costs will be decisive for future use and the recyclability of particle-reinforced aluminum alloys. In particular, the profitability of potential recycling technologies will depend on energy consumption and  $CO_2$  emissions. The energy consumption for recycling aluminum alloys is about 95% lesser than the energy used in primary production.<sup>23</sup> However, the potential cleaning processes must compensate for existing problems such as the emergence of impurities and the low wettability of the SiC particles within the melt, as these result in a detrimental effect on the properties of the recycled material.<sup>1,6</sup> Moreover, not every reinforcement phase is compatible with every matrix alloy, whereby intermediate phases, such as  $Al_2O_3$  (mostly in the form of films), spinel, or  $MgAl_2O_4$ , can occur at the SiC or  $Al_2O_3$  matrix interface (as very fine  $<2\mu m$  crystals),<sup>5</sup> and may adversely affect the recyclability. The removal of inclusions by metal melt filtration with simple 10 pores per inch (ppi) ceramic foam filter (CFF) in gravity casting leads to a consistent improvement of yield strength and Young's modulus (an increase of about 30-40%), as well as in the ductility of the composite.<sup>5</sup> Furthermore, the application of 10 ppi CFF made of zirconium oxide (Stalex, Feseco) similarly resulted in the effective removal of non-metallic inclusions from austenitic steel castings (FeMnAl steels).<sup>24,25</sup> Besides non-metallic inclusions, liquid inclusions can be also removed by 10 ppi magnesia-stabilized zirconia foam filter from stainless steel 316 melt.<sup>26</sup> The highest detected filtration efficiency of non-metallic inclusions was 41%.<sup>25</sup> Higher removal efficiency of 95% for large alumina inclusions from steel alloys was reported by Raiber et al.<sup>27</sup> using 25 ppi CFFs.

The removal of extrinsic inclusions from particle-reinforced Al alloys is quite different compared to steel alloys due to their thermophysical properties related to the viscosity and processing of the liquid MMCs. The processing of particle-reinforced Al alloys comprises a variety of adjustable parameters in the stir casting process. However, other potential recycling technologies also exist. While the stir casting is influenced by its complexity of variables,

such as geometry and position of the stirrer, stirring parameters (time and rotational speed), as well as melt temperature and the particle characteristics,<sup>7,10</sup> a specially patented process by Keßler et al.<sup>16</sup> eliminates this complexity. The potential technique prevents the dewetting and settling effect of SiC particles and also reduces the gas and/or oxide input into the melt. Another advantage, besides the reduced gas and oxide input, is the reduction of costs compared to conventional melting technology for particle-reinforced material.<sup>28</sup>

Thereby, the patent document (DE 19906939 C2, 2002)<sup>28</sup> includes the utilization of an induction crucible furnace with several sub-coils and direct inductive heating in combination with a low-pressure die casting process. The induction coils are applied at a high frequency (greater than or equal to 500 Hz) for melting and at a low frequency (lesser than 50 Hz) for holding and stirring, allowing a precise control of the melting process.<sup>28</sup> However, due to the utilization of predefined extrusion billets, the melt volume is merely limited to low-volume melt batches ( $\approx 12.5$  kg), as the coupling conditions of these billets are the most beneficial for an application.<sup>29</sup> Consequently, the potential recycling technologies must be economical regarding the production costs, the recycling capability of particle-reinforced Al alloys, and the profitability. Even though the global MMC market demand in terms of production volumes is expected to increase to 12,842.5 tons (revenue: \$558.5 million) in 2027, according to future forecasts.<sup>19</sup>

Due to the growing proportion of the global market demand and the low availability of technologies for recycling SiC-reinforced Al, the recovery of foundry recycled material and scrap is becoming more important. The increasing margins of MMCs require developing effective recycling technology of particle-reinforced alloys regarding the tending higher danger of contamination of conventional Al alloys due to their accidental application by insufficient scrap sorting, separation, or transportation. Therefore, this paper focuses on the recycling capability of three different weight fractions of SiCp in particle-reinforced aluminum alloys to replicate scrap mixtures of

different origins (both classical Al alloys and composites) according to the real recycling process where different mixed chemical compositions may occur. Typical applications of SiC-reinforced AMCs are attributed to be between 5 and 20 wt% of SiC particles due to the prevention of inherent viscosity issues.<sup>7</sup> The potential recovery capability by filtering out SiC particles from metal matrix composites offers small and middle-sized enterprises (SMEs) the opportunity to purify contaminated melt compositions without using special equipment (stirring tools for continuous mixing), even in the normal casting production cycle. The separation of SiC particles is hence realized by metal melt filtration using 20 ppi CFFs. For this purpose, numerical simulation, as well as filtration and remelting trials, is performed, and investigated for different filter materials.

## Experimental Section

### Castings and Materials

As base materials, Duralcan<sup>TM</sup> from RioTinto Alcan (Canada)<sup>9</sup> and pure aluminum Al99.7-E (Rheinfelden, Germany)<sup>30</sup> were used to generate alloy compositions of three different weight fractions of SiCp. Duralcan<sup>TM</sup> generally consists of a metal matrix of an AlSi9Mg with 20 wt% of SiC particles (marked as alloy designation I/20 wt% SiC). The chemical compositions are shown in Table 1.

The alloys with different weight fractions of SiC particles were prepared in a medium-frequency induction furnace (43 kW, 50 Hz) with a volume of  $\approx 4$  kg. Accordingly, the Duralcan<sup>TM</sup> aluminum alloy (AA359/SiC/20p) was melted first at  $\approx 745$  °C, and then the pure aluminum Al99.7-E was added to adjust the different weight fractions. To prevent the formation of aluminum carbide (Al<sub>4</sub>C<sub>3</sub>), it is necessary to control the melt temperature.<sup>10</sup> Considering that Becker et al.<sup>31</sup> detected a high wetted (1-2  $\mu$ m thick) Al<sub>4</sub>C<sub>3</sub> layer in sessile drop experiments on a SiC filter substrate with an Al alloy at temperatures up to 900 °C, a precise control of the bath temperature of the melt is

**Table 1. Chemical Composition of the Alloys (Weight Fractions are the Average Value of Three Individual Values) in Optical Emission Spectrometer (OES) SPECTROMAXx (Ametek, USA). The Si Content Represents the Total Concentration of the Two Including Compounds (matrix and SiC particles). The Pouring Temperature is Measured by Thermocouple of Type K**

Alloy	Si [%]	Fe [%]	Cu [%]	Mn [%]	Mg [%]	Zn [%]	Ti [%]	Al [%]	Temp.
Al99.7-E	0.205	0.261	0.0082	0.013	0.0044	0.0110	0.082	Bal.	n/a
I/20 wt% SiC	20.78	0.282	0.0130	0.043	0.417	0.0032	0.080	Bal.	744 °C
II/10 wt% SiC	8.17	0.173	0.0064	0.009	0.143	0.0022	0.027	Bal.	744 °C
III/5 wt% SiC	3.31	0.197	0.0065	0.009	0.0086	0.0060	0.018	Bal.	751 °C

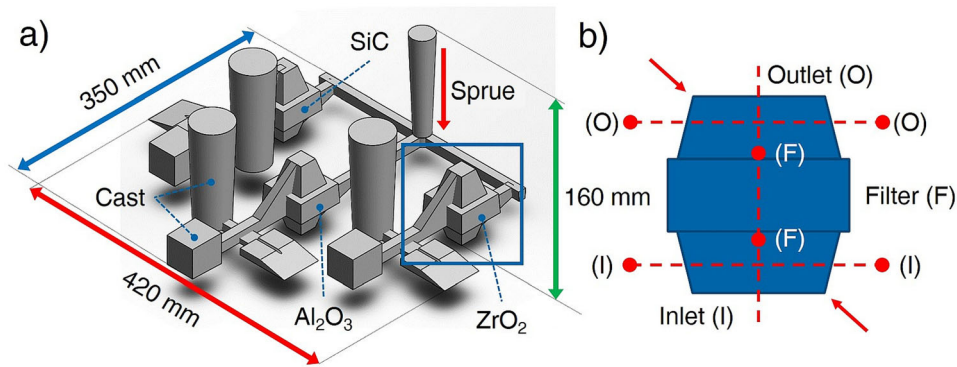


**Figure 1. Illustration of the (a) CAD model with dimensions used for furan resin-bonded sand molds in gravity casting with (b) the sampling scheme of the specimens (from the region marked in the blue box) of inlet (I) and outlet (O) on the 20 ppi foam ceramic filter (marked with arrows), as well as the cross-section of the half of the ceramic foam filter (F). Cuts are marked with dashed lines and letters.**

inevitable to avoid the formation of aluminum carbides. Furthermore, the SiC particles are not thermodynamically stable and degrade the fluidity of the molten AMC. Hence, overheating above 830 °C shall be prevented.<sup>8,14</sup> Keßler et al.<sup>16</sup> reported that this reaction is already starting at  $\approx 750$  °C in an AlSi9 alloy, whereas in addition to the temperature also the holding time and Si content must be considered. Additionally,  $Al_4C_3$  is water soluble and consequently not detectable in the water-based metallographic preparation. Subsequently, the prepared alloys with different weight fractions were poured into a special three-chamber mold made of furan resin-bonded sand for filtration trials. This specially developed three-chamber design is shown in Figure 1a and allows a uniform filling of the mold with consistent flow conditions for the filtration process. In each chamber, a 20 pores per inch (ppi) ceramic foam filter (CFF) was placed. The used filter materials were  $Al_2O_3$  (Hofmann Ceramic, Germany), SiC, and  $ZrO_2$  (both of Foseco Foundry Division, Germany).

In addition, trials were performed to investigate the influence of remelting process on the recycling capability. For this purpose, 3.5 kg of the base material (Duralcan™: I/20 wt% SiC) was used. Therefore, the behavior of the SiC particles was observed during multiple remelting tests (4 cycles) at  $\approx 745$  °C in the medium-frequency induction crucible furnace (43 kW, 50 Hz). After each cycle, a rod sample ( $\varnothing$  30 mm, height 120 mm) made in furan resin-bonded sand was cast for metallographic analysis. The residual liquid material was then remelted, and the procedure was repeated.

## Numerical Simulation

The simulation was carried out by the program Magmasoft, version 5.4.2. (MAGMA Gießereitechnologie GmbH, Germany) to demonstrate uniform filling conditions and

flow lengths in the exposed model system. Simulation parameters were set as casting in a furan mold made from silica sand with 2.0 wt% of furan (binder). Initial mold properties included a sand porosity of 40.0%, a permeability of 100.0  $cm^3/min$ , and a sand mold temperature of 20 °C. As casting material, the Al matrix alloy (according to ISO 3522: AlSi9Mg, corresponds to A359.0) with a pouring temperature of 745 °C and a time of 6.16 s were selected. The pouring time  $\tau$  was calculated by the equation according to Sobolev-Dubickij.<sup>32,33</sup>

$$\tau = k \cdot (w_G \cdot m_G)^{1/3} \quad \text{Eqn. 1}$$

$m_G$  was determined from the volume  $V$  given from the CAD file with 900  $cm^3$ . The density  $\rho$  of 2.68  $g/cm^3$  of the matrix alloy is given by the data sheet.<sup>9</sup>  $w_G$  is the critical wall thickness of 8 mm, predefined from the CAD file, and the material-dependent factor  $k$  was specified with 2.3.<sup>32,33</sup> The mass has to be stated in kilograms. In each filter chamber, a SiC ceramic foam filter of square-shaped geometry was placed for the simulation. The heat transfer coefficient between casting and sand mold, as well as filter material and mold, was given from the standard database of Magma ( $\alpha = 400$   $W/m^2 \cdot K$ ). The thermophysical properties were predefined with  $\lambda = 0.7$   $W/m \cdot K$  (in the range of 400-650 °C) and  $c_p$  of max. 1285  $J/kg \cdot K$  (at 573 °C) from the Magma database. The mold design was specially developed based on the insights gained from the literature.<sup>34,35</sup>

## Analytical Methods

Chemical analyses were performed using an optical emission spectrometer (OES) SPECTROMAXx (Ametek, USA), where the average of three individual measured values was used for establishing the chemical composition. For microstructural investigations, the specimens were cut as a cross-section from regions of the inlet (I) and outlet

(O) of the gating system, where the 20 ppi filters were placed. A cross-section of the CFF was also analyzed (see Figure 1b). All samples were polished to the final stage with colloidal silica suspension OP-U by a semi-automatic grinding and polishing machine, TegraPol-31 (Struers, Germany). For determining the area fractions of SiC particles, image analyses using Stream Motion software (Olympus, Japan) were conducted in a predefined region of interest (ROI) with a magnification of 100 times. Therefore, panoramic images were taken by a Keyence VHX 2000 digital microscope with a VH-Z100 R objective (Keyence, Japan). The area fraction of particles (SiCp) can be calculated as the mathematical proportion or ratio of a fraction based on a grayscale value to a total predefined region of interest (ROI area). Microstructure characterization was also performed by a scanning electron microscope (SEM; VEGA3 W-REM, Tescan, Germany) employing secondary electron (SE) and backscattered electron (BSE) imaging, as well as measurements (mappings) regarding elemental distribution using energy-dispersive X-ray spectroscopy (EDS; XFlash 610 M detector, Bruker Nano, Germany). The analytical methods were also used in preliminary studies for the detection of iron-rich intermetallic phases.<sup>36</sup>

## Results and Discussion

### Simulation

According to the incomplete database for Al alloy composites due to undefined interactions between the extrinsic non-metallic inclusions and the metallic melt, Magmasoft simulates and visualizes the filling behavior, heat transfer, and temperature field during the filling process of the 3-chamber mold before the proper casting trials concerning the matrix-base alloy. In Figure 2, the simulation results of air entrapment, absolute velocity, and pouring temperature at different pouring times (0.493 and 3.604 s) demonstrate uniform flow conditions during the filling process. A relatively uniform and low-turbulence inflow can be seen in the gate and filter area. Figure 2a and b show the air entrapment and absolute velocity, where the molten metal starts filling the chambers, and where the initial contact occurs between the melt and the CFFs. It can be noted that the midstream of the mold is reaching an absolute velocity of more than 1.0 m/s, resulting in a higher percentage of air entrapment ( $\geq 4.00\%$ ) during the filling of this filter chamber. The values of more than 4.00% in air entrapment indicate potentially enshrouded air pockets by the fluid. Thereby, the air entrapment of more than 5.00% constitutes a considerable critical value for a finite element in the meshing of the system. Regarding the absolute velocity, the critical value of 0.5 m/s is given from the literature.<sup>37,38</sup> In this case, the criterion is the critical Reynolds number, where the inertial forces of the fluid are disrupted, and the surface tension forces will be transcended, leading to an

overturning effect and turbulences at the melt front.<sup>38</sup> In the literature, the critical value of  $Re_{crit} \geq 2300$  is frequently reported, which is derived by measurements of Julius Rotta.<sup>39</sup> However, a relatively low-turbulent velocity in the inflow region on the CFF of nearly 0.5 m/s can be inferred from Figure 2b. Other studies recommended this critical velocity in dissimilar alloy systems such as Fe-Mn-Al steels to minimize air entrapment and reoxidation defects.<sup>24,25</sup> Thereby, 10 ppi zirconia foam filters (Stalex, Foseco) were used with a predefined pouring time, providing that a longer filling time resulted in higher air entrainment and slower filling rate, which created premature solidification defects, such as cold shuts or misruns.<sup>25</sup> Contrarily, shorter filling time led to a higher absolute velocity and more turbulences.<sup>25</sup> In the present case, the higher absolute velocity in the casting runner of the model system can be attributed to the non-existent change in the direction of the melt. Furthermore, the nearly low-turbulent inflow resulted in wetting of the CFFs with an approximately constant flow length and temperature ( $\geq 722$  °C, see Figure 2c). The castings behind the filter chamber also showed an approaching consistent temperature field (between 626 and 713 °C), indicating a temperature close to the liquidus temperature (626.33 °C) of this alloy system according to Luo et al.<sup>40</sup> The uniform mold filling conditions behind the filter are emphasized by the absolute velocity at pouring time of 3.604 s (Figure 2d), as the CFF further act as velocity or flow modifier, resulting in a continuous velocity of below 0.5 m/s.

In preliminary studies on filtration efficiency using computational fluid dynamics (CFD) simulations, predictions of the flow behavior between the experimental and simulation results were performed on a composite material. Here, simulations were conducted on Al<sub>2</sub>O<sub>3</sub> particles in an AlSi7Mg matrix alloy.<sup>34,35</sup> For this purpose, different positions and types (ppi numbers) of CFFs were considered. The horizontally rising filter position for 20 and 30 ppi showed the most efficient separation rate, and neither the particle size nor type (alumina or spinel) of inclusions significantly influenced the filtration efficiency due to the similar contact angle and wettability between inclusions and the molten metal.<sup>34,35</sup> The three-chamber furan mold was specially designed for this position gained from these insights.

### Filtration Tests

The element contents of the chemical composition of the different weight fractions of SiCp are shown in Table 1. The chemical analysis was detected in the OES by sparking on rapidly solidified externally samples. The measurements contained the SiC particles, as well as the metal matrix of the AlSi9Mg alloy. Theoretically, the silicon content (Si) is supposed to be represented by the two measured compounds in addition, but hereby Si was about 20.8 wt%.

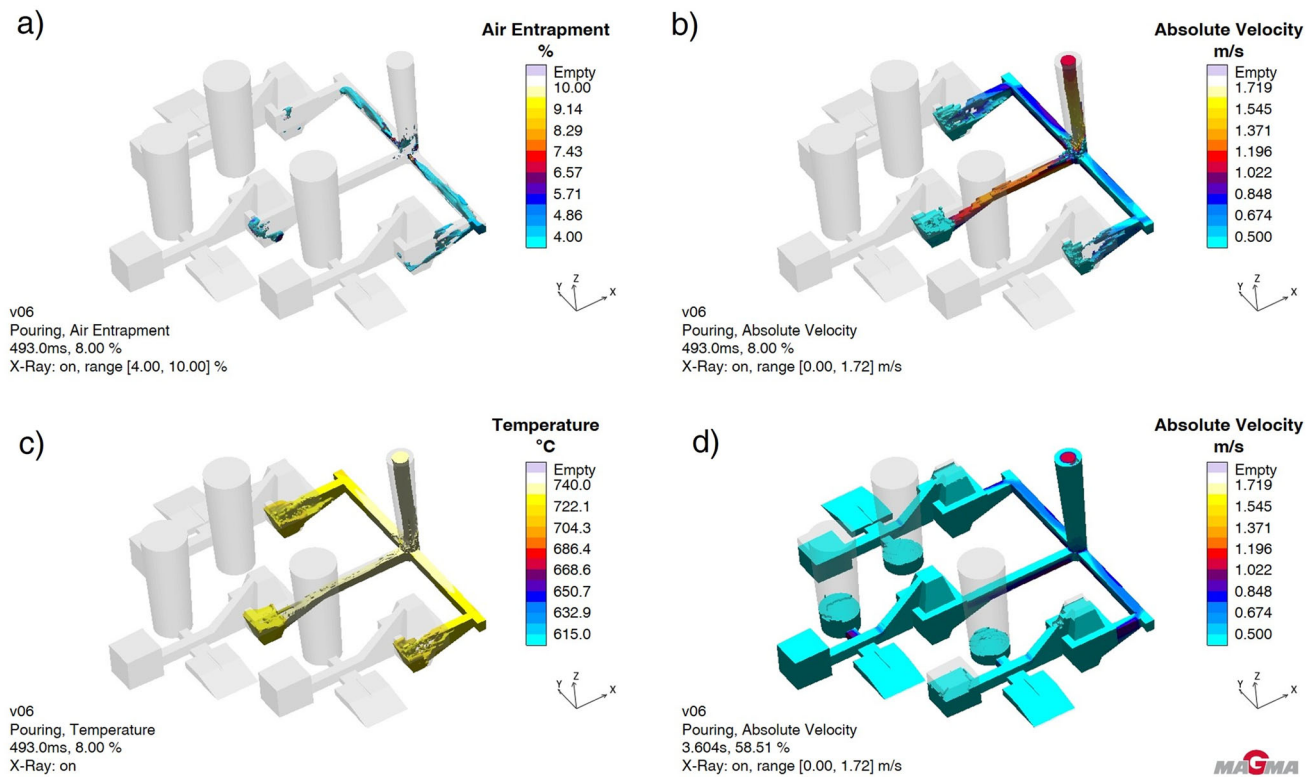


**Figure 2. Illustration of the flow lengths of molten aluminum in the three-chamber mold with (a) air entrapment (in the range of 4.0-10.0%), (b) absolute velocity (above the critical velocity of 0.5 m/s), and (c) temperature at a pouring time of 0.493 s, as well as (d) the absolute velocity at 3.604 s in the Magmasoft simulation program (version 5.4.2.). The mold cavity is depicted transparently with an activated X-Ray.**

However, the chemical analysis can be affected by the distribution of the particles, thus sparking by the OES on a concentrated section with a higher amount of SiCp may increase the detected Si content. Conversely, a lower SiCp fraction causes a lower Si content.

The investigated 20 ppi CFFs made of  $\text{Al}_2\text{O}_3$ , SiC, and  $\text{ZrO}_2$  material were placed as previously marked for each filtration trial in the filter chambers. Figure 3 represents a cross-section of the sample of the outlet region on the  $\text{Al}_2\text{O}_3$  CFF. The mathematical method for detecting the area fractions of the SiC particles (i.e., the object area percentage) is done on polished micrographs (seen in Figure 3). For this purpose, the predefined regions of interest (ROIs) are marked with blue boxes (numbers 1-3) in the panoramic image of the cross-section of the outlet on the  $\text{Al}_2\text{O}_3$  filter to obtain an average value. For comparison, the area fractions of the different filter materials by a consistent value (particles through square  $\mu\text{m}$ ), the three regions (1-3) were detected by an approximately constant ROI area ( $\mu\text{m}^2$ ). The individual values were 2174320.4  $\mu\text{m}^2$  (ROI 1), 2176709.7  $\mu\text{m}^2$  (ROI 2) and 2164762.9  $\mu\text{m}^2$  (ROI 3). The averaged ROI areas are listed in Table 2. The area fractions of SiC particles were then achieved by image analysis in the mentioned regions of interest (ROIs) with the same magnification of 100 times in the light microscopy. Therefore, the object area percentage

(SiCp) can be calculated as a mathematical proportion or ratio of the summarized areas of particles (as a partial sum of a finite geometric series) based on a grayscale value to a predefined ROI area ( $\mu\text{m}^2$ ). As a result, the area fraction (marked in red in Figure 3) is obtained, which is 15.99% on average and composed of the individual values 17.03% (ROI 1), 14.62% (ROI 2), and 16.34% (ROI 3). The area fraction of nearly 16% correlates relatively well with the 20 wt% of the base alloy (Duralcan<sup>TM</sup>). An example of the area fractions from the inlet and outlet of a CFF is given in Figure 4, where the detected regions of the particles (marked in red) are also represented at 100x magnification in addition to the panoramic images (left sides).

Figure 4a represents the cross-section of the sample from the inlet and Figure 4b the outlet section on the  $\text{Al}_2\text{O}_3$  CFF of alloy III with 5 wt% SiCp. A significant reduction of SiC particles can be observed in the micrographs. Whereas the mean area fraction of SiC particles in the inlet is about 6.11%, a particle content of 0.10% on average was detected in the sample of the outlet. This indicates a significant removal of SiC particles by metal melt filtration through the 20 ppi filter, thus allowing the determination of the filtration efficiency for the ceramic foam filter by comparing the two sections. Accordingly, the filtration

Filtermaterial: Al<sub>2</sub>O<sub>3</sub> – Outlet (O) | ROI Ø: 15.99 %

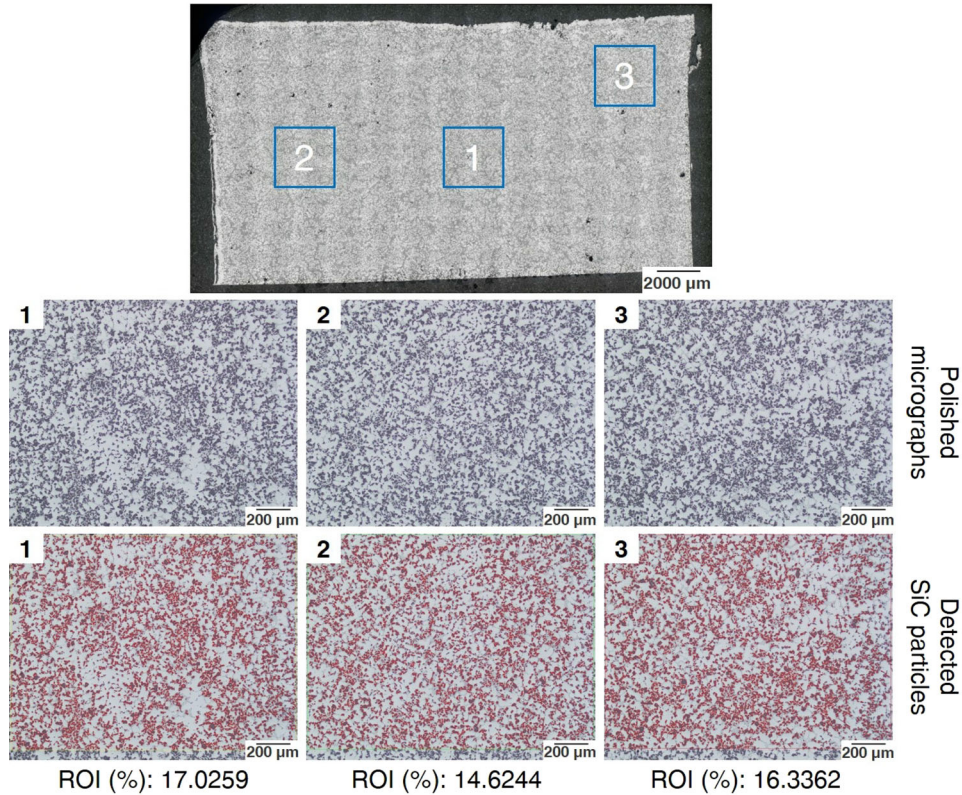


**Figure 3.** Determination of the area fraction of SiC particles in a specimen of a cross-section in alloy designation I with 20 wt% SiCp in the outlet section (O) using the 20 ppi Al<sub>2</sub>O<sub>3</sub>-filter (top: panoramic image) by means of three measured regions of interests (ROI) on polished samples marked in blue boxes with numbers 1 to 3 (middle). Detected SiCp in the three ROIs based on a grayscale marked in red with the values of the area fractions (bottom).

efficiency can be calculated from the area fractions (or a number of particles) of the inlet and outlet using the equation below.<sup>34,35</sup> This allows a comparison of the removal rates of the three different filter materials:

$$E = \frac{A_0 - A_1}{A_0} \cdot 100[\%] \quad \text{Eqn. 2}$$

$A_0$  indicates the area fraction of SiC particles from the inlet and  $A_1$  the area fraction from the outlet section, whereby the filtration efficiency of alloy designation III in Figure 4 is consequently 98.4% on average. The results of filtration efficiencies are listed in Table 2. Measurements of inclusion area fractions at the filter inlet and outlet side were also obtained by automated feature analysis (AFA) using an Aspec Pica 1020 with energy-dispersive X-ray spectroscopy for alumina inclusions in a 316 stainless steel casting.<sup>25</sup> The highest inclusion removal efficiency (defined by  $E$  or  $\eta$ ) was 41%.<sup>25</sup> Furthermore, it is found that the prediction of filtration efficiency is directly proportional to the initial inclusion concentration,<sup>26</sup> implying that the three different initial weight fractions of SiCp generated by the dilution with pure aluminum are

expected to have a significant effect on the filtration efficiency.

Table 2 contains the measurement results from the image analysis of the different weight fractions of SiC particles for the three filter materials. In each case, the average values of area fraction ( $\bar{\phi}$ ), as well as the area of the region of interest (ROI area in  $\mu\text{m}^2$ ), and the filtration efficiency are given. The ROI areas are in the range of 2.15 to 2.18  $\text{mm}^2$ , indicating a relatively constant area value for comparing the detected particles. A decreasing trend is noticeable between the individual measurements of the area fractions from the inlet and outlet for the different ceramic foam filters. Thus, according to Eqn. 2, the filtration efficiency can be determined for each filter material. The highest filtration efficiency of  $\approx 22\%$  is achieved by the Al<sub>2</sub>O<sub>3</sub> and ZrO<sub>2</sub> filter in the base material (trial I/20% SiCp). Likewise, high filtration efficiency of about 98% is also shown by the Al<sub>2</sub>O<sub>3</sub> and ZrO<sub>2</sub> filter at 5 wt% SiCp (trial III). The 20 ppi SiC filter exhibits the lowest filtration efficiency for SiC particles removal of about 7 and 93%. In particular, the detected value of 1.50% in the outlet region of the SiC filter corresponds to a densified region of SiC particles at 5 wt% SiCp. However, the individual values

**Table 2. Values of the Area Fractions of SiC Particles Using Image Analysis from the Cross-Section Before (inlet) and After (outlet) the 20 ppi Ceramic Foam Filter on the Three Different Filter Materials. The Filtration Efficiency E was Calculated according to Eqn. 2 with the Average Values ( $\bar{\emptyset}$ ) of the Three Individual Measurements with  $A_0$  (Values of the Cross-section Before) and  $A_1$  (After) the Ceramic Foam Filter**

Alloy	Filter material	ROI	Particle area percentage (%)				ROI area ( $\mu\text{m}^2$ ) $\bar{\emptyset}$	Efficiency E (%)	
			1	2	3	$\bar{\emptyset}$			
I/20 wt% SiCp	$\text{Al}_2\text{O}_3$	Inlet (I)	20.04	19.53	20.92	20.16	2166558.7	20.68	
		Outlet (O)	17.03	14.62	16.34	15.99	2171931.0		
	SiC	Inlet (I)	17.94	17.79	16.92	17.55	2173924.4		6.78
		Outlet (O)	15.45	17.30	16.33	16.36	2150684.1		
	$\text{ZrO}_2$	Inlet (I)	19.16	17.71	18.35	18.41	2158413.6		22.60
		Outlet (O)	13.31	15.21	14.23	14.25	2154646.0		
II/10 wt% SiCp	$\text{Al}_2\text{O}_3$	Inlet (I)	6.18	7.65	7.06	6.96	2172928.4	n/a	
		Outlet (O)	n/a	n/a	n/a	n/a	n/a		
	SiC	Inlet (I)	12.05	12.59	13.07	12.57	2166562.0		n/a
		Outlet (O)	n/a	n/a	n/a	n/a	n/a		
	$\text{ZrO}_2$	Inlet (I)	9.40	10.63	10.65	12.23	2168351.2		n/a
		Outlet (O)	n/a	n/a	n/a	n/a	n/a		
III/5 wt% SiCp	$\text{Al}_2\text{O}_3$	Inlet (I)	6.30	5.83	6.19	6.11	2169741.3	98.36	
		Outlet (O)	0.10	0.12	0.09	0.10	2169146.4		
	SiC	Inlet (I)	5.71	7.62	7.88	7.07	2158052.5		92.64
		Outlet (O)	1.50	0.04	0.03	0.52	2174918.9		
	$\text{ZrO}_2$	Inlet (I)	4.83	6.87	7.02	6.24	2175321.0		98.40
		Outlet (O)	0.10	0.07	0.12	0.10	2174716.9		

can vary considerably in some cases, as the values between 1.50 and 0.03% clearly show. The average value of the three individual measurements provides therefore an appropriate degree of statistical certainty for determining the filtration efficiency. Accordingly, the separation of inclusions on similar filter surfaces cannot be confirmed, despite being reported in the literature.<sup>41</sup> Based on the findings in Table 2, no filtration efficiency was determined for the weight fraction of 10 wt% SiCp (trial II) in this study. This was due to incomplete mold filling during casting. The metal flow is interrupted throughout the filling process, which could have been caused by a critical ratio between the MMC and pure Al addition. Strikingly, the molds of the base composite alloy (20 wt% SiCp) and the relatively high diluted alloy composition (trial III) with 5 wt% SiCp were completely filled. In this case, an extremely high initial SiC concentration did not lead to higher filtration efficiency, whereas the results appeared to be strongly affected by the initial viscosity. At equivalent temperature, the viscosity with 5 wt% SiCp is much lower than with 20 wt% due to the lower amount of particles. Therefore, the SiCp are considerably finely dispersed in trial III under relatively high dilution (according to Figure 4a). Consequently, in spite of introducing a relatively high degree of oxides by the addition of pure Al, the CFF exhibits its almost complete filtering performance and thus removes a significantly high proportion of SiC particles.

Furthermore, superheating of  $\approx 90$  K above 660 °C (pure Al) was documented for alloy III, so a temperature-related effect on the viscosity might be negligible. However, the 50/50 addition of base composite alloy and pure aluminum led to an inappropriate effect or critical ratio between the amount of SiC particles and the introduced oxides, resulting in an interruption of mold filling. Accordingly, the cross-sections of the half filter widths are examined by light microscopy. The microscopic images show a clogging of filter bridges by agglomerates in the inflow area of the CFFs (see Figure 5).

Section 6 (in Figure 5a) shows agglomerated SiC particles, which are also present in a similar size (as agglomerates) in the other filter materials (SiC and  $\text{ZrO}_2$ ) at alloy II with 10 wt% SiCp. Consequently, these agglomerates cause a clogging effect on the filter bridges in all filter materials, which is visible as well in section 5 in Figure 5b. Furthermore, a distinct filter cake (with an increased density of particles) is evident in the inflow region in the panoramic image for all filters. This indicates an abrupt interruption in the mold filling process. Noticeable is also the region of the agglomerated SiC particles in the  $\text{ZrO}_2$  filter (see in Sect. 2 in Figure 5c). Here, the filter's permeability has changed. The permeability is strongly affected by the deposition of inclusions.<sup>34</sup> In this case, more aggregated SiC particles penetrate into the porous cell structure, which manifests as



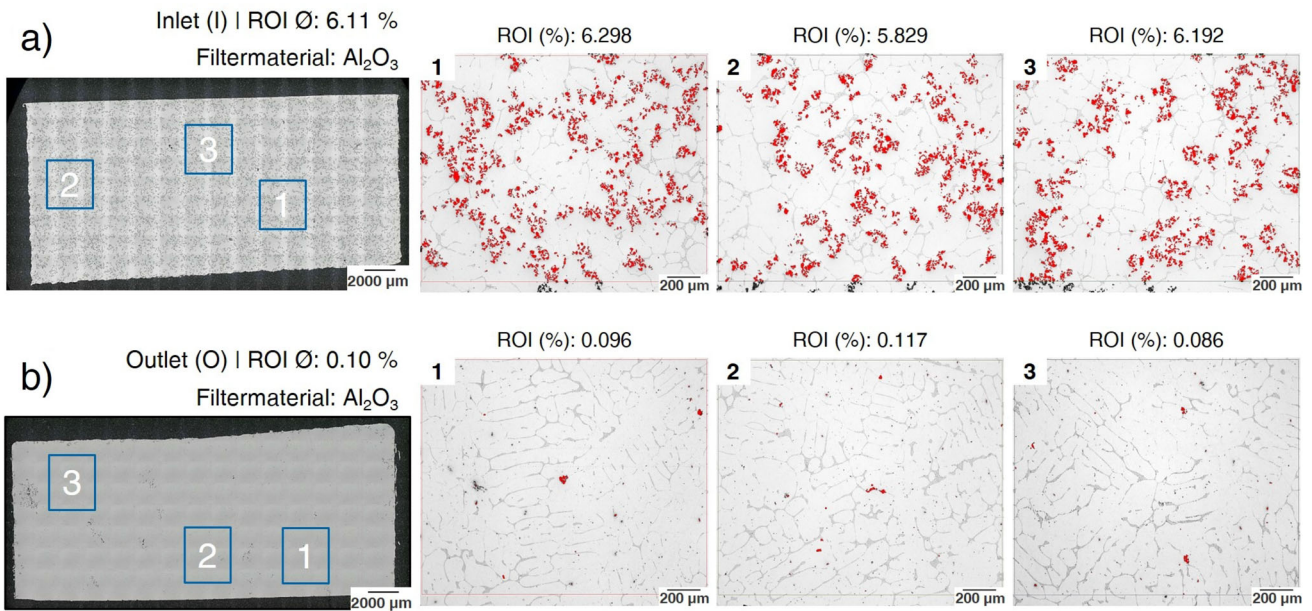


**Figure 4.** Determination of the area fraction in alloy designation III with 5 wt% SiCp on a cross-section of (a) inlet and (b) outlet section on the 20 ppi Al<sub>2</sub>O<sub>3</sub>-filter (left sides) by means of three detected regions of interests (ROI) marked in blue boxes with numbers 1 to 3. Detected SiCp in the three ROIs based on a greyscale marked in red with the individual values of the area fractions (above).

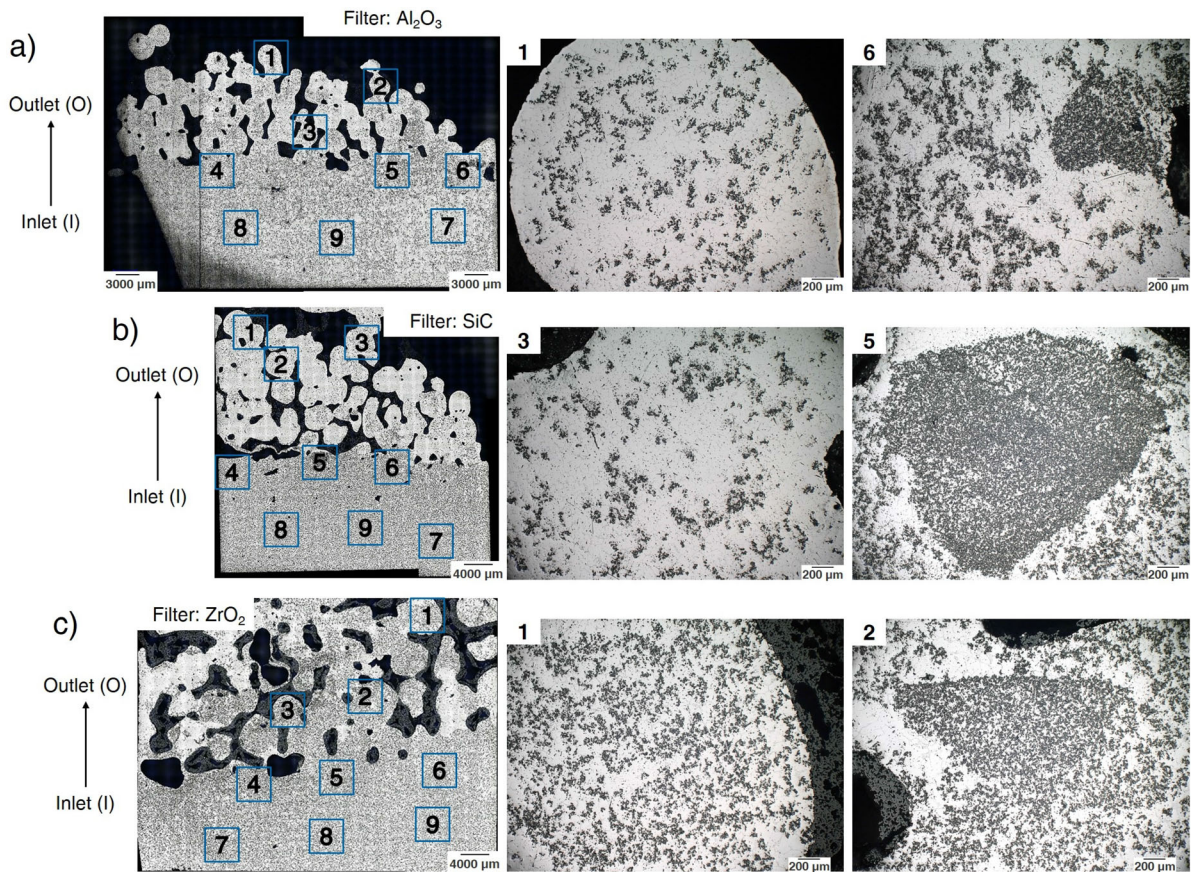


**Figure 5.** Illustrations of the 20 ppi ceramic foam filter (CFF) on alloy designation II with 10 wt% SiCp of the panoramic images (left side) for the three different filter materials: (a) aluminum oxide (Al<sub>2</sub>O<sub>3</sub>), (b) silicon carbide (SiC), and (c) zirconium oxide (ZrO<sub>2</sub>). The micrographs with 100x magnification to determine the area fractions of the SiC particles are marked in blue boxes with the numbers 1 to 9.

**Table 3. Values of Area Fractions and Numbers of SiC Particles Using Image Analysis from the Cross-section of Half of the 20 ppi Ceramic Foam Filter (CFF) on the Three Different Filter Materials. The Detected Regions of Interest (ROIs) are Numbered 1 to 9 in Blue Boxes in Fig. 5**

Alloy	Filter material	SiCp	Particle area percentage (%)								
			1	2	3	4	5	6	7	8	9
II/10 wt% SiCp	Al <sub>2</sub> O <sub>3</sub>	ROI	8.71	9.30	8.56	15.72	18.49	20.22	8.86	11.07	11.19
		No.	1720	1633	1909	2898	3258	2516	1903	2208	2585
	SiC	ROI	4.25	5.15	8.59	14.31	20.46	19.43	15.65	16.17	15.69
		No.	1320	1581	2053	3754	7549	3371	3331	3618	4072
	ZrO <sub>2</sub>	ROI	13.08	19.80	17.80	20.33	20.98	18.32	20.03	19.78	18.63
		No.	3750	3900	3251	4399	3706	3996	4084	3149	3394

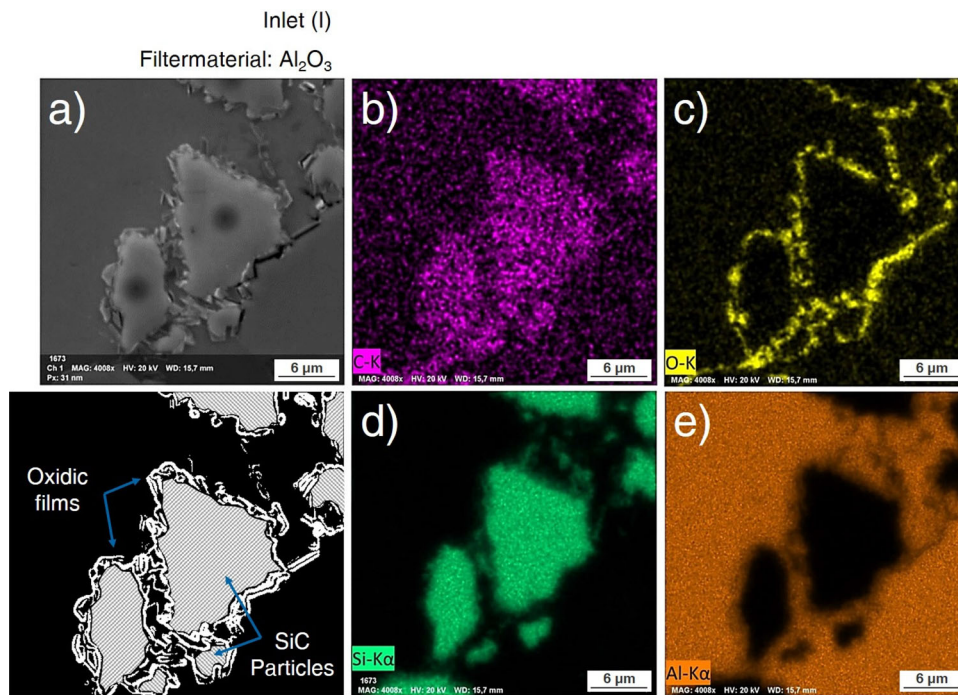
areas with an increased particle density between the filter bridges. A possible reason for this could have been an interchange of the position of the ZrO<sub>2</sub> CFF with the Al<sub>2</sub>O<sub>3</sub> filter, as the progressive penetration of the SiC agglomerate could have been a consequence of the higher ingate velocity seen in the simulation in Figure 2b. Additionally, the melt in the outlet area of the ZrO<sub>2</sub> CFF was able to emerge but did not completely fill the cavity behind. Furthermore, the addition of pure aluminum to the Duralcan<sup>TM</sup>, which was mixed half and half, led to the formation of agglomerated SiC particles by introducing more oxidic films and inclusions, theoretically. Therefore, no determination of the filtration efficiency was evaluated in trial II with 10 wt% SiCp. Nonetheless, the cross-sections of the CCFs were analyzed by light microscopy. The results are listed in Table 3.

Table 3 shows the detected area fractions (represented as particle area percentage) and numbers (or amount) of SiC particles. The numbers 1 to 9 are marked in the blue boxes for determining the regions of interest (ROIs) in the panoramic images in Figure 5 (left sides). Using the Al<sub>2</sub>O<sub>3</sub> filter, for example, a high number (2516 to 3258) and thus a higher particle area percentage (15.72 to 20.22%) of SiC particles appear in the inflow region, representing the described filter cake in Sects. 4-6. Sections 7-9 constitute the inlet region, whereas Sects. 1-3 depict the filter's interior areas. Except for the previously described ZrO<sub>2</sub> CFF, the area fraction and amount of SiC particles tend to decrease. It was already explained that Sects. 1-3 have a higher amount and area fraction in the ZrO<sub>2</sub> filter. Otherwise, the values range from 8.56 to 9.30% (Al<sub>2</sub>O<sub>3</sub>) and 4.25 to 8.59% (SiC). The sections of the inflow region (7-9) also tend to be lower in area fraction and number than Sects. 4-6, providing that merely Al<sub>2</sub>O<sub>3</sub> CFF reflects the theoretical weight fraction of the adjusted particle-reinforced alloy composition II in this zone (with 8.86 to 11.19%). Hence, a massive accumulation of SiC particles before the respective filters indicated a distinct filter cake. The agglomeration of SiC particles can possibly be caused by oxide films, which commonly occur in particle-reinforced

Al alloys, as reported in the literature.<sup>38,42,43</sup> Therefore, scanning electron microscope (SEM) images were taken to investigate interaction effects between the reinforced particles and the metallic matrix under energy-dispersive X-ray spectroscopy (EDS) (Figure 6).

Figure 6a shows the SEM images in secondary electron contrast (SE) of a section of the inlet (I) from the Al<sub>2</sub>O<sub>3</sub> filter of alloy III with 5 wt% SiCp. There, SiC particles are visible in an Al matrix. At the edges of the respective particles, visible and enclosed layers appeared around the surfaces of the reinforcement phase. A key factor for uniform properties of AMCs is the wettability of the reinforcement phase with the matrix, which is the ability of the liquid metal to spread on the solid surface of the SiC particles.<sup>10</sup> Figure 6b to e illustrates the elemental distribution in EDS maps to determine the localization of the elements carbon (C), oxygen (O), silicon (Si), and aluminum (Al). Accordingly, the elemental distribution of C and Si indicates the SiC particles, while the element O indicates an oxide film around the respective SiCp, and Al represents the aluminum matrix. As mentioned by Samuel & Samuel,<sup>5</sup> an intermediate phase of Al<sub>2</sub>O<sub>3</sub> in the form of a few μm thick film is shown in Figure 6, implying that no wetting of SiC particles occurred in alloy III (containing 5 wt% SiCp) due to the excessive addition of pure aluminum. However, the oxide layers would explain the relatively high filtration efficiency of the SiC particles on the Al<sub>2</sub>O<sub>3</sub> filter, as well as the low efficiency on the SiC filter, and thus Al<sub>2</sub>O<sub>3</sub>-based CCFs are recommended for further investigations to separate recycled mixed alloy compositions.

Generally, no wetting occurs when the contact angle of the particles (or inclusions) is between 90° and 180°. According to previous studies,<sup>34,35</sup> bonding mechanism of Al<sub>2</sub>O<sub>3</sub> particles to the aluminum matrix was investigated in an AlSi7Mg0.3 alloy. Furthermore, Duralcan<sup>TM</sup> was also used to introduce non-metallic inclusions (as particles). In this case, a contact angle of 152° resulted in no theoretical wetting of the Al<sub>2</sub>O<sub>3</sub> particles,<sup>44</sup> whereas SEM



**Figure 6.** SEM image in (a) SE contrast from the cross-section of the inlet (I) of Fig. 4a with a schematic illustration of entrapped oxide films on interfaces of SiC particles (below), as well as EDS maps to determine the elemental distribution of (b) carbon (C), (c) oxygen (O), (d) silicon (Si), and (e) aluminum (Al). The elemental distribution of C and Si corresponds to the SiC particles, while the element O represents an oxide layer around the respective SiCp, and Al represents the aluminum matrix.

examinations revealed an adherent Mg layer as a coating around the respective reinforcement particles.<sup>34,35</sup> Regarding the contact angle of SiC with molten Al, Becker et al.<sup>31</sup> observed a strongly decreasing wetting angle after a longer holding period ( $\approx 3$  h). Finally, they determined a relatively small contact angle of  $\approx 70^\circ$ , while the Al-Si melt was in contact with a SiC filter substrate for more than 120 min. This indicates that the wetting angle and thus the wettability are affected merely by time. However, a contact angle of about  $150^\circ$  was also detected at the beginning of the sessile drop experiments,<sup>31</sup> which means a generally low wettability at the initial contact between both compounds. In addition, during the entire melting process in the induction crucible furnace, the liquid was not allowed to rest at any time to prevent a settling effect.

Due to the absolute velocity (of more than 1.0 m/s) in the midstream of the mold (see Figure 2b), where the Al<sub>2</sub>O<sub>3</sub> filter was normally located, the local turbulence may have caused the formation of the visible oxide films in SEM images. In Figure 6, a schematic illustration of the entrapped oxide films at the interfaces of SiC particles is shown. Divandari & Campbell<sup>43</sup> reported on the oxide film characteristics in an AlSi7Mg alloy for analyzing the dynamic conditions in castings. The entrainment of newly created oxide films in the bulk of molten Al occurs when a dry surface adheres to an opposing dry surface as a double

folded oxide film (better known as bifilms) that is finally wetted by the melt.<sup>37,42</sup> The inner, unwetted surface in the liquid represents an unbound interface as a folded oxide film, resulting from the turbulent transfer of the molten Al in common casting operations or from turbulent conditions during mold filling (as seen previously).<sup>37,43</sup> These double folded oxide layers (or bifilms) are schematically illustrated on the surface of the SiC particles by blue arrows in Figure 6. Likewise, turbulent filling conditions can cause the formation of bifilms also in dissimilar alloys, since the occurrence of extensive bifilms consisting of aluminum and manganese oxides in the inlet region of a 10 ppi CFF has been detected in FeMnAl steels.<sup>24</sup>

The literature described the entrainment of folded oxides by penetrating the melt surface from the outside via exogenous particles (SiCp) or non-metallic inclusions.<sup>38,42</sup> As aluminum immediately forms an oxidic film of alumina by contact with the atmosphere, any turbulence at the surface leads to the formation of entrapped bifilms (through melt motion). This implies three potential causes of these defects on the extrinsic inclusions: turbulence due to (a) mold filling, (b) melt transport, and (c) melting technology. In this context, the low wettability of the SiC particles with the melt can be explained by the formation of oxidic bags (also known as paper bags), in which the particles are enshrouded by the oxide layers and separated

by an air pocket, so that the entrained particles are not submerged in the molten metal.<sup>38,42</sup> The entrainment of particles of smaller size (such as SiC with a diameter of lesser than 125-140  $\mu\text{m}$ )<sup>6,17</sup> occurs in agglomerates, which has also been established previously and commonly observed during the manufacture of metal matrix composites (MMC) even in the stir casting process.<sup>42</sup> For this purpose, melting technologies with the potential objective for the processing and purification of particle-reinforced aluminum alloys are recommended.

One of them is the utilization of a crucible induction furnace with several sub-coils and direct induction heating.<sup>28,29</sup> The individually selectable sub-coils allow a reduced input of oxides and further inclusions due to a special melt bath treatment. However, in this study, the referred process technology was not available to the authors for investigations, since a conventional medium-frequency induction crucible furnace was used, that did not allow any control of sub-coils. The relatively high frequency of melting ( $\approx 7000$  Hz) resulted in an enhanced heat input into the melt but not in a stronger stirring effect to retain the SiCp in suspension. Furthermore, the adverse position of the ingot material led to the floating of the material portion that had not been liquefied. In conventional melting technology for induction crucible furnaces, the melt front rises from the bottom to the top during melting, allowing the residual solid fraction to float up unhindered.<sup>29</sup> Consequently, this material breaks through and permanently destroys the oxide layer on the bath surface. Due to the electromagnetic field, the residual portions are set in rotation around their own axes. The strong rotational motion leads to the constant formation of new oxide surfaces and therefore explains the entrainment of oxidic defects such as double folded, unbounded non-metallic surfaces (depicted in Figure 6), according to the literature.<sup>37,38,42,43</sup> Once the rest of the solids are melted on the bath surface, the persistent turbulences create the potential for the formation of mixed oxides (e.g., spinels),<sup>29,41</sup> which also promote the entrainment of these oxides into the melt.

Another appropriate purification technology is the combined or hybrid stirring method to maintain the SiCp in suspension. Considering the computational fluid dynamics results (Ansys CFD), the authors obtained a uniform dispersion of SiCp with a homogeneity of 75% using the combined stirring method.<sup>7</sup> This method consists of both mechanical and ultrasonic stirring.<sup>7</sup> However, since the dispersion of SiC particles was merely shown numerically, the filtration efficiency in the practical trials of this study would be decreased due to the increased accumulation of SiCp in the inlet region of the CFF, leading to a possible clogging effect, which was observed previously (Figure 5). For this purpose, centrifugal forces could be applied in a round filter housing to remove these agglomerates. Due to

the tangential ingate of the housing, the clogging of a cylindrical CFF placed in the centre can be avoided by ensuring that the filter bridges are unclogged by SiC particles of larger size classes ( $\geq 200$   $\mu\text{m}$ ). Using the simple geometry of round filter housings with an appropriate initial casting velocity, the SiC agglomerates can be retained by the inertial or centrifugal forces, while the particles of smaller size classes can be effectively separated from the residual molten material via the CFF.

## Remelting Tests

To investigate the influence on the recycling capability due to remelting of the composite material, rod specimens were cast according to the geometry shown in Figure 7a. For this purpose, the same base material with 20 wt% SiCp was melted and solidified several times. The recyclability is limited due to the viscosity of the liquid MMC, as particle-depleted and particle-rich zones are formed during melting and solidification, as described in the literature.<sup>5,8,17,29</sup> As the SiCp are not retained in suspension (segregation), this adversely affects the casting and mechanical properties.<sup>1,6</sup> This results from the low wettability of the SiC particles, leading to an increasing viscosity in the particle-rich zone. Consequently, the particles in this zone become more bound to each other due to internal friction and might be less moveable. This leads to a relatively strong accumulation effect of SiC particles.

Figure 7b constitutes the micrograph of the polished rod sample of the base material with 20 wt% SiCp after the first melting process (cycle 1). The micrograph depicts finely distributed SiC particles in an almost dendritic structure of the Al matrix alloy. The determined area fraction of this sample is 15.75%, with an averaged ROI area of 2.175  $\text{mm}^2$ , which is comparable to the values of the base material in Table 2. After each cycle of melting, an increasing accumulation of SiC particles is observed, with an increase in area fraction from 20.28% to 28.32% from the 2nd to the 3rd cycle (Figure 7c). After the 3rd time of remelting the same material (cycle 4), the area fraction was 30.18%, retaining a mushy slime-like residual material in the induction crucible furnace after sampling. Finally, in the remelted residual material, the area fraction was 35.16% (here designated as sludge, Figure 7d). The mean ROI areas ranged from 2.147 to 2.175  $\text{mm}^2$ . The higher area fraction indicates an increasing accumulation of SiC particles after each remelting cycle of the same material, which means that Al alloys reinforced with SiC particles cannot be reused and recycled as often as desired. Sharma et al.<sup>17</sup> also observed a strong settling effect during remelting of composite casting scrap. Herein, the settling rate was strongly dependent on the particle size and weight fraction of SiC particles. However, even these parameters are significantly affected by remelting of the same

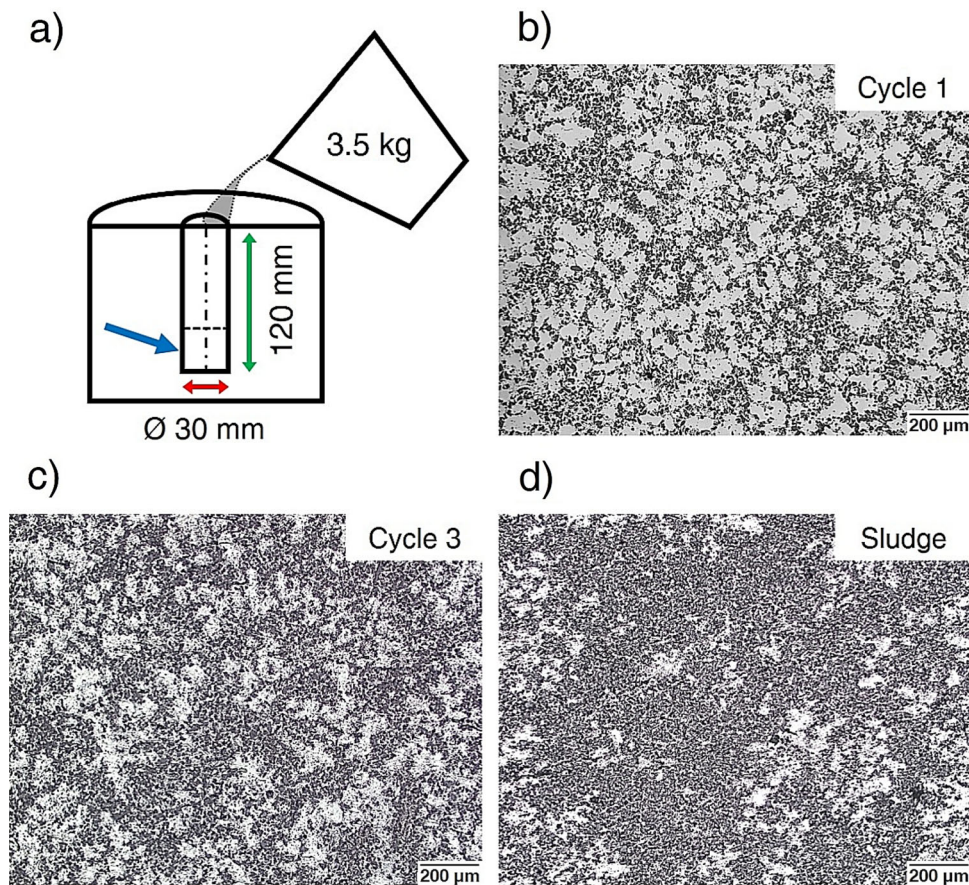


**Figure 7.** Illustrations of the (a) sampling scheme, as well as the polished specimens (taken from the section marked with a blue arrow) for determining the area fractions on a cross-section of the rod samples for different cycles of the remelting tests: (b) origin material (20 wt% SiCp), (c) after remelting two times, and (d) residual material in the crucible (presented as sludge).

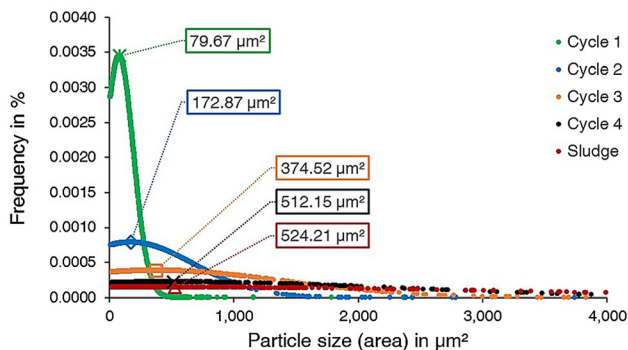


**Figure 8.** Illustration of the frequency (in %) plotted over the normal distribution of particle size, aligned to the detected SiC particles and area fractions (in  $\mu\text{m}^2$ ) obtained via image analysis. Mean values of the normal distribution curves are marked in the respective boxes, which refer to the respective cycle of the remelting trials (cf. in Fig. 7).

reinforcing material, increasing the weight fraction in some sections, as reflected in the increased area fractions, as well as in the particle size (see Figure 8).

Figure 8 represents the relative frequency plotted against the normal distribution of particle size aligned to the detected SiC particles and their individual area fractions (in  $\mu\text{m}^2$ ). The individual values of area fraction (or particle size) are plotted as single points for each melting cycle (marked in colors), which are previously illustrated in Figure 7. Likewise, the marked boxes indicate the respective mean values for each cycle. However, the dot plot merely depicts the density function of the normal distribution  $N(\mu, \sigma^2)$  and not the distribution functions of the individual cycles themselves. Here, an expectation value  $\mu$  (in this case the mean value) and a defined standard deviation are predetermined from the image analysis data. The standard deviation  $\sigma$  describes the width of the normal distribution. Thus, the standard deviation can be assigned to a simple relevance regarding the magnitude of the occurring probabilities or frequencies. Therefore, the displayed Y-values are frequencies (in %). Concerning the dot plot, an increasing mean value (particle size) is revealed by each additional melting cycle, with the relative frequency dropping from 0.0035% initially to below 0.0005%. The mean value increases concurrently from 79.67 to 524.21  $\mu\text{m}^2$  in the sludge, indicating a strong accumulation effect

by means of the steadily flattening curve of the density function after the reuse of the same material. Consequently, an infinite reuse of the SiC particle-reinforced material cannot be confirmed, meaning that the recycling capability and reuse of AMC's are limited due to the strong agglomeration or accumulation effect in the induction crucible furnace. Therefore, advanced melting technologies have to be used for processing and recycling these composite materials. The AMC's cannot be processed without an appropriate stirring technique; otherwise, the particles will not be maintained in suspension. Nevertheless, according to these results of particle size and distribution curves, an increasingly strong accumulation effect occurred, despite the usage of electromagnetic fields in the induction crucible furnace.

## Conclusion

The concluding remarks can be drawn from this study as follows:

- (1) The simulation results reveal uniform flow conditions during mold filling with a relatively low-turbulent absolute velocity in the inflow region on the ceramic foam filters (CFF), resulting in their wetting with an approximately constant flow length, temperature, and velocity.
- (2) The filtration efficiency increased by decreasing the weight fraction from 20% to 5% of SiC particles (SiCp), achieving a significant particle reduction of more than 90%. The 20 ppi SiC filter exhibited the lowest filtration efficiency for the removal of SiCp. Therefore, Al<sub>2</sub>O<sub>3</sub> and ZrO<sub>2</sub> filters are recommended for the filtration process at lower weight fractions of SiC particles.
- (3) Investigations on CFFs of alloy composition of 10 wt% of SiCp have shown a clogging effect on the filter bridges by SiCp agglomerates through a changed permeability. The metal flow interruption during mold filling occurred due to the introduction of oxides by the addition of pure aluminum.
- (4) The interactions between the reinforcement phase (SiCp) and aluminum matrix (Al) show oxide layers around the respective SiC particles in the scanning electron microscope (SEM) with energy-dispersive X-ray spectroscopy (EDS). Hence, this indicates a generally low wettability of the SiCp, caused by the entrapped oxide films at the interfaces between the reinforced particles and the metal matrix.
- (5) Moreover, an increasing accumulation of SiC particles with an increased mean value (particle size) was observed, indicated by a steadily flattening curve of the density functions after each additional remelting cycle of the same

composite material in the crucible induction furnace. Therefore, the recycling capability is limited to advanced melting and recycling technologies, since the SiC particle-reinforced Al alloys cannot be reused and recycled as frequently as desired. In particular, the application of a simple geometrically designed filtration housing with an internal tubular filter can potentially achieve almost complete recovery of the aluminum matrix.

## Acknowledgements

The authors would like to acknowledge the German Research Foundation (DFG, Deutsche Forschungsgemeinschaft) for funding this work and the project as a part of the Collaborative Research Centre 920 "Multi-Functional Filters for Metal Melt Filtration – A Contribution towards Zero Defect Materials" (Project ID: 169148856 – SFB 920, Subproject T03). Particular acknowledgment is expressed to the commitment of the staff members of the Foundry Department, especially Ms. Mrówka, Mr. Genthe, and Mr. Khan Mohammed, for their assistance in the realization of this work.

## Funding

Open Access funding enabled and organized by Projekt DEAL. Open access funding enabled and organized by Projekt DEAL.

## Data Availability

The data of this study are available from the corresponding author on a reasonable request.

**Conflict of interest** The authors declare no conflict of interest.

**Open Access** This article is licensed under a Creative Commons Attribution 4.0 International License, which permits use, sharing, adaptation, distribution and reproduction in any medium or format, as long as you give appropriate credit to the original author(s) and the source, provide a link to the Creative Commons licence, and indicate if changes were made. The images or other third party material in this article are included in the article's Creative Commons licence, unless indicated otherwise in a credit line to the material. If material is not included in the article's Creative Commons licence and your intended use is not permitted by statutory regulation or exceeds the permitted use, you will need to obtain permission directly from the copyright holder. To view a copy of this licence, visit <http://creativecommons.org/licenses/by/4.0/>.

## REFERENCES

1. O. Beffort, *Metallmatrix-verbundwerkstoffe: eigenschaften, anwendungen und bearbeitung*. 6. Int. IWF-Kolloquium über Feinstbearbeitung technischer Oberflächen. <https://www.dora.lib4ri.ch/empa/>

- [islandora/object/empa:9924](#) (2002). Accessed 11 April 2022
2. K. Gawdzińska, R. Łapawa, P. Szymański, A. Bejger, K. Nozdrzykowski, Characteristics of production methods of aluminium and magnesium matrix composite castings. *Mechanika* **90**(3/18), 285–296 (2018)
  3. Y. Nishida, Recycling of aluminum matrix composites. *Adv. Eng. Mater.* **3**(5), 315–317 (2001)
  4. Y. Nishida, N. Izawa, Y. Kuramasu, Recycling of metal matrix composites. *Metall. Mater. Trans. A* **30**, 839–844 (1999)
  5. A.M. Samuel, F.H. Samuel, Foundry aspects of particulate reinforced aluminum MMCs: factors controlling composite quality. *Key Eng. Mater.* **104–107**, 65–98 (1995). <https://doi.org/10.4028/www.scientific.net/KEM.104-107.65>
  6. J. Eliasson, R. Sandström, Applications of aluminium matrix composites. *Key Eng. Mater.* **104–107**, 3–36 (1995). <https://doi.org/10.4028/www.scientific.net/KEM.104-107.3>
  7. U. Aybarc, H. Yavuz, D. Dispinar, M.O. Seydibeyoglu, The use of stirring methods for the production of SiC-reinforced aluminum matrix composite and validation via simulation studies. *Int. J. Met.* **13**(1), 190–200 (2019). <https://doi.org/10.1007/s40962-018-0250-3>
  8. D.M. Schuster, M.D. Skibo, R.S. Bruski, R. Provencher, G. Riverin, The recycling and reclamation of metal-matrix composites. *JOM* **45**, 26–30 (1993)
  9. Rio Tinto Alcan, RT-Aluminium-Duralcan-fact-sheet-2.pdf. <https://www.riotinto.com/-/media/Content/Documents/Products/Aluminium/RT-Aluminium-Duralcan-fact-sheet.pdf?rev=48ac3c3132294b6cbc5921e6c15aef3d> (2014). Accessed 21 May 2021
  10. C. Bulei, M.P. Todor, I. Kiss, Metal matrix composites processing techniques using recycled aluminium alloy. *IOP Conf. Series Mater. Sci. Eng.* **393**, 012089 (2018). <https://doi.org/10.1088/1757-899X/393/1/012089>
  11. M. Łagiewka, C. Kolmasiak, Composite centrifugal castings after remelting. *Metalurgija* **60**(3–4), 441–443 (2021)
  12. A. Lohmüller, C. Rauber, Partikelverstärkte magnesium- oder aluminiumlegierung. *DepatisNet*. <https://depatisnet.dpma.de/DepatisNet/depatisnet?action=pdf&docid=DE102006023041B4&xxxfull=1> (2007). Accessed 18 March 2022
  13. B. Stojanovic, L. Ivanovic, *Application of aluminium hybrid composites in automotive industry*. *Teh. Vjesn.* **22** (1), 247–251 (2015). <https://doi.org/10.17559/TV-20130905094303>
  14. H. Kaufmann, E. Neuwirth, R. Kretz, Einfluss von filtern auf die mechanischen eigenschaften der SiC-partikelverstärkten aluminiumlegierung AlSi9Mg: Teil 1. *Statische materialkenndate*. *Giesserei* **80**(11), 351–354 (1993)
  15. H. Kaufmann, E. Neuwirth, R. Kretz, C. Henkel, Einfluss von filtern auf die mechanischen eigenschaften der SiC-partikelverstärkten aluminiumlegierung AlSi9Mg: Teil 2. *Dynamische materialkenndate*. *Giesserei* **81**(10), 289–293 (1994)
  16. A. Keßler, D. Brungs, O. Brandt, X. Wirth, M. Seidenschwang, M. Dette, Leistungs- und entwicklungspotential der SiC-partikelverstärkten aluminiumlegierung am beispiel gegossener bremscheiben. *Nichtmetalle in Metallen*, 93–100 (2000)
  17. A. Sharma, B. Ahn, Recycling of aluminum alloy from Al-Cu metal matrix composite reinforced with SiC particulates. *Korean J. Mater. Res.* **28**(12), 691–695 (2018). <https://doi.org/10.3740/MRSK.2018.28.12.691>
  18. Transparency Market Research (TMR): Metal matrix composites (MMC) market for ground transportation, electronics/thermal management, aerospace and other end-users - global industry analysis, size, share, growth, trends and forecast, 2013–2019. <https://www.transparencymarketresearch.com/metal-matrix-composites.html> (2014). Accessed 07 October 2021
  19. Grand View Research: Metal matrix composite market size, share & trends analysis report by end-use (ground transportation, electronics), by product (refractory, aluminum), by region, and segment forecasts, 2020 - 2027. <https://www.grandviewresearch.com/industry-analysis/metal-matrix-composites-mmc-market> (2020). Accessed 08 October 2021
  20. Market Research Future (MRFR): Metal matrix composites (MMCs) market: information by product type (aluminum, nickel, refractory, copper and others), end-use industry (aerospace & defense, automotive, building & construction, marine, electronics, healthcare and others) and region. <https://www.marketresearchfuture.com/reports/metal-matrix-composites-mmcs-market-8131> (2021). Accessed 07 October 2021
  21. Research Nester: Metal matrix composites market segmentation by product type (aluminum MMC, superalloy MMC, nickel MMC, copper MMC, and others); by end-use industry (transportation, aerospace, thermal/electronics management, marine, and others) - global demand analysis. <https://www.researchnester.com/reports/metal-matrix-composites-market/1024> (2021). Accessed 07 October 2021
  22. Duralcan USA: Duralcan composite casting guidelines. VIII-1, San Diego, California (1990)
  23. Umweltbundesamt: factsheet-aluminium\_fi\_barrierefrei.pdf. *Umweltbundesamt*. [http://www.umweltbundesamt.de/sites/default/files/medien/3521/dokumente/factsheet-aluminium\\_fi\\_barrierefrei.pdf](http://www.umweltbundesamt.de/sites/default/files/medien/3521/dokumente/factsheet-aluminium_fi_barrierefrei.pdf) (2019). Accessed 02 September 2021
  24. K. Balasubramanian, L.N. Bartlett, R. O'Malley, S. Chakraborty, M. Xu, Filtration efficiency of inclusions in lightweight FeMnAl steels. *Int. J. Met.* **14**(2), 328–341 (2020). <https://doi.org/10.1007/s40962-019-00372-7>

25. S. Chakraborty, R.J. O'Malley, L. Bartlett, M. Xu, Removal of alumina inclusions from molten steel by ceramic foam filtration. *Int. J. Met.* **15**, 1006–1020 (2021). <https://doi.org/10.1007/s40962-020-00537-9>
26. S. Chakraborty, R.J. O'Malley, L. Bartlett, Ceramic foam filter micropores as sites for liquid inclusion retention. *Int. J. Met.* **16**(1), 20–34 (2022). <https://doi.org/10.1007/s40962-021-00585-9>
27. K. Raiber, P. Hammerschmid, D. Janke, Experimental studies on Al2O3 inclusion removal from steel melts using ceramic filters. *ISIJ Int.* **35**, 380–388 (1995). <https://doi.org/10.2355/isijinternational.35.380>
28. M. Dette, A. Keßler, D. Brungs, Induktionstiegelofen und dessen verwendung zum herstellen von gußteilen aus partikelverstärkten aluminium- und magnesiumlegierungen. *DepatisNet*. <https://depatisnet.dpma.de/DepatisNet/depatisnet?action=pdf&docid=DE000019906939C2&xxxfull=1> (2000). Accessed 13 December 2021
29. A. Keßler, M. Dette, D. Brungs, Schnelles induktives schmelzen partikelverstärkter aluminiumlegierungen. *Giessereiforschung* **53**(1), 15–24 (2001)
30. Rheinfelden Alloys GmbH & Co. KG: Verarbeitungsdaten\_RHEINFELDEN-ALLOYS\_2015\_DE. [https://rheinfelden-alloys.eu/wp-content/uploads/2016/01/Verarbeitungsdaten\\_RHEINFELDEN-ALLOYS\\_2015\\_DE.pdf](https://rheinfelden-alloys.eu/wp-content/uploads/2016/01/Verarbeitungsdaten_RHEINFELDEN-ALLOYS_2015_DE.pdf) (2015). Accessed 08 April 2022
31. H. Becker, B. Fankhänel, C. Voigt, A. Charitos, M. Stelter, C.G. Aneziris, A. Leineweber, Interaction of Fe-containing, secondary Al-Si alloy with oxide and carbon-containing ceramics for Fe removal. *Adv. Eng. Mater.* **24**(2), 2100595 (2022). <https://doi.org/10.1002/adem.202100595>
32. G.M. Dubickij, *Cast Metals Research Journal*, vol. 10–11 (American Foundrymen's Society, USA, 1974), p.14
33. G.M. Dubickij, *Litnikovye sistemy* (Maschgez, Moscow-Swerdlowsk, 1951)
34. E. Jäckel: Einfluss von filterstruktur und gießsystem auf die filtrationseffizienz im aluminiumformguss. Eds.: Wolf, G., Aneziris, C.G., TU Bergakademie Freiberg, PhD thesis (2019)
35. B. Baumann, A. Keßler, E. Hoppach, G. Wolf, M. Szucki, O. Hilger, Investigation of particle filtration in aluminium alloy. *Arch. Foundry Eng.* **21**(3), 70–80 (2021). <https://doi.org/10.24425/afe.2021.138668>
36. J.P. Schoß, H. Becker, A. Keßler, A. Leineweber, G. Wolf, Removal of iron from a secondary Al-Si die-casting alloy by metal melt filtration in a laboratory filtration apparatus. *Adv. Eng. Mater.* **24**(2), 2100695 (2022). <https://doi.org/10.1002/adem.202100695>
37. M. Hemmati, M. Divandari, The effects of oxide film characteristics on the bubble damage defect in Al5Mg and Al7SiMg alloys. *Proceedings of Iran International Aluminum Conference: IIAC* (2012)
38. J. Campbell, Entrainment defects. *Mater. Sci. Technol.* **22**(2), 127–145 (2006). <https://doi.org/10.1179/174328406X74248>
39. J. Rotta, Experimenteller beitrag zur entstehung turbulenter strömung im rohr. *Ing. Arch.* **24**, 258–281 (1956)
40. X. Luo, Y. Han, Q. Li, X. Hu, Y. Li, Y. Zhou, Effect of pouring temperature on microstructure and properties of A356 alloy strip by a novel semisolid micro fused-casting for metal. *J. Wuhan Univ. Technol.-Mat. Sci. Ed.* **34**, 1205–1209 (2019). <https://doi.org/10.1007/s11595-019-2179-7>
41. C. Voigt, E. Jäckel, F. Taina, T. Zienert, A. Salomon, G. Wolf, C.G. Aneziris, P. Le Brun, Filtration efficiency of functionalized ceramic foam filters for aluminium melt filtration. *Metall. Mater. Trans. B* **48**, 497–505 (2017). <https://doi.org/10.1007/s11663-016-0869-5>
42. J. Campbell, Cavitation in liquid and solid metals: role of bifilms. *Mater. Sci. Technol.* **31**(5), 565–572 (2015). <https://doi.org/10.1179/1743284714Y.0000000581>
43. M. Divandari, J. Campbell, Oxide film characteristics of Al7SiMg alloy in dynamic conditions in casting. *Int. J. Cast Met. Res.* **17**(3), 182–187 (2004). <https://doi.org/10.1179/136404604225017546>
44. L.N.W. Damoah, L. Zhang, Removal of inclusions from aluminum through filtration. *Metall. Mater. Trans. B* **41**(4), 886–907 (2010). <https://doi.org/10.1007/s11663-010-9367-3>

**Publisher's Note** Springer Nature remains neutral with regard to jurisdictional claims in published maps and institutional affiliations.